ESA Contract: "Mars Climate Database: Validation and Improvements for Surface Operations"

Ref: ESA Contract No. 4000128572/19/NL/AS

WP2 - Deliverable Document D2 - Part 1:

Finalization of the GCM version 6

Improving the Dust Cycle

Prepared by: Antoine Bierjon, Ehouarn Millour, François Forget

Laboratoire de Météorologie Dynamique, CNRS, IPSL, Paris, France.

October 4, 2022

Contents

Introduction

This document reviews the improvements concerning the modeling of the dust cycle in the version 6 of the Mars Planetary Climate Model (PCM), formerly called the LMD Mars Global Climate Model. This version is abbreviated as "GCMv6" in the following, while "GCMv5" refers to the reference version of the model that has been used for the building of the Mars Climate Database version 5.3. The main areas of improvement from the GCMv5 dust cycle were the dust vertical distribution, especially forming and maintaining *dust detached layers* in the tropics, and the diurnal cycle, which was hindered by a daily renormalization.

The previous report from 2019[1], referred to as *TN_Dust_2019* in the text below, detailed three main parametrizations that control the new GCMv6 dust cycle.

The first one is the revisited dust injection scheme, meticulously driven by observational scenarios. It replaces the former GCMv5 two-step approach consisting of a unrealistically huge constant near-surface injection, followed by a strong renormalization of the column to match the observations. The second keystone of this new dust cycle consists in the mesoscale phenomenon of the *rocket dust storms*, revealed by Spiga et al. [2013] and very active in the dusty season. It was implemented in the GCM by Chao Wang (Wang et al. [2018]) and Margaux Vals, and profoundly reshapes the dust vertical profile. The last part was another mesoscale process, induced by the sub-grid scale topography's updraft slope winds, which concentrate aerosols on top of the mountains and enable dust to follow a rocket dust storm-like local ascension. This process, more simply called the *mountain top flows*, has been parametrized by Margaux Vals during her PhD thesis.

Sections 1, 2, 3, reintroduce these three parametrizations and highlight the tuning and changes made since *TN_Dust_2019*.

To these main processes implemented to simulate the dust cycle in GCMv6, we also add a refinement of the dust optical depth forcings, whose conversion from infrared to visible happens to be very sensitive to the dust effective particle size. **Section 4** presents our work about the space and time variability of this conversion coefficient and its impact on our simulations.

Section 5 details the small correction we make in the radiative transfer concerning dust aerosols. Indeed, unlike GCMv5 that renormalized the Column-integrated Dust Optical Depth (CDOD) to the daily observational forcings, the CDOD in GCMv6 can slightly departs from the scenario baseline. We thus put a safeguard, in the radiative transfer only, to limit the possible thermal impact of an erroneous simulated dust opacity. The way we coded this correction still allows for a dust diurnal evolution, which was one of the main improvements in the new GCMv6 compared to GCMv5.

Finally, **Section 6** shortly introduces the parametrization of the scavenging of the aerosols by the CO_2 snow. This process was at first implemented to take into account its impact on the dust particles in the polar night, but its effect appears to be predominant for the water cycle, so it will be mainly described in the *Deliverable Document D2 - Part 2 : Improving the Water Cycle*.

All these changes in the model enable us to simulate a dust cycle that seems closer to the observations by multiple aspects, as detailed in **Section 7**, and on which we base the version 6.1 of the Mars Climate Database.

[1]ESA Contract No. 44000122721, Work Package 4, Technical Note 6, Part 1: *Improved Dust Cycle*

1 Dust injection scheme

The new dust injection scheme, developed in 2017 by Deborah Bardet (see *TN_Dust_2019*), takes as an input a prescribed column-integrated dust optical depth (CDOD), which is compared to the optical depth computed by the GCM. Usually, the prescribed CDOD is taken from daily mapped scenarios made by Luca Montabone (see Montabone et al. [2015], Montabone et al. [2020], or the Mars Climate Database website). These scenarios cover Martian Years from MY24 to MY35, and consist of daily maps on a regular horizontal grid gathering the observations from different instruments (TES[2], THEMIS[3], MCS[4]) which are then extrapolated to cover the whole planet via a kriging procedure, and are normalized to a reference surface pressure of 610 Pa.

We consider the scenarios representative of the certain local time of 14h (2pm), which is close from the daytime Mean Solar Local Time of the heliosynchronous orbits of the instruments. Note that this assumption on the scenario local time only affects the amplitude of the diurnal CDOD evolution in the GCM, and not its phasing which is controlled by the dynamics and the physical processes. Indeed, when a local grid point of the model reaches this local time, we compute the difference between the current $\tau_{\text{pref,gcm}}$ and the $\tau_{\text{pref,scenario}}$ from the next Martian day (or sol) at 14h. The difference, if positive (more dust in the observations than in the model), is interpreted as the trigger of a dust storm, and leads to the injection in the first atmospheric layer of a specific tracer, the *stormdust*, distinct from the usual *background dust*. The conversion from the visible (VIS) CDOD difference $\Delta\tau$ into the dust flux $d_t q$ (in $\text{kg}_{\text{dust}}.\text{m}^{-2}.\text{s}^{-1}$), injected from the surface in the lowest atmospheric layer to reach the prescribed column one sol later, is made via the following relationship :

$$d_t q = C_{\text{inj}} \times \frac{4\, p_{\text{surf}}\, \rho_{\text{dust}}\, r_{\text{eff}}}{3\, p_{\text{ref}}\, Q_{\text{ext}}\, \Delta t} \Delta\tau \tag{1}$$

with p_{surf} the local surface pressure (in Pa) and p_{ref} the reference pressure (610 Pa) ; ρ_{dust} the dust density, r_{eff} the effective radius and Q_{ext} the VIS extinction coefficient of the injected dust distribution (resp. fixed at $2500\text{kg}_{\text{dust}}.\text{m}^{-3}$, 3µm and 2.4). $\Delta t = t_{\text{end of inj.}} - t_{\text{start of inj.}}$ (in s) is the local time interval during which the dust injection is performed at a constant rate. A tunable coefficient C_{inj} is also added to qualify the injected dust flux. Indeed, when injecting dust in a given GCM column, the dust that is missing to match the scenario CDOD one sol later can simply come by transport from adjacent columns, and hence require no local lifting. Conversely, dust sedimentation and transport outside of the injection column should also be accounted for. We tuned this coefficient to match the observations of VIS CDOD (scenarios) but also the dust vertical profiles from MCS (Kleinböhl et al. [2009]). In the current version of GCMv6 used for the production of MCD6.1, C_{inj} =0.25.

We also explored the sensitivity of the injection timing on the creation of dust detached layers. If narrow temporal windows, like 8h-10h or 10h-12h, seem more efficient at raising dust

[2] *Thermal Emission Spectrometer* (Christensen et al. [2001]), onboard Mars Global Surveyor (MGS)
[3] *Thermal Emission Imaging System* (Christensen et al. [2004]), onboard Mars Odyssey (ODY)
[4] *Mars Climate Sounder* (McCleese et al. [2007]), onboard Mars Reconnaissance Orbiter (MRO)

via very concentrated rocket dust storms, this induces a too strong dust amount being sustained in the atmosphere compared to MCS. Wider intervals like 10h-14h can dampen this effect while still maintaining some dust in mid-altitude. However, since no clear physical justification supports those narrow injection timings, the lifting window was widen again, firstly to 8h-18h to follow the Planetary Boundary Layer average activation time, and finally to the full sol (0h-24h). Studies like Chatain et al. [2021] also presented evidence for some nighttime local turbulence near the surface, motivating us further to keep the possibility of active dust lifting at any local time of the sol. Technically, stormdust is still injected at night, as during daytime, but is very quickly detrained into background dust as there is then no sunlight to make it ascend (see **Section 2**). The near-surface layers of the GCM fill up with dust, part of which sediments while the rest can be entrained upwards as soon as a true rocket dust storm forms in the morning.

2 Rocket dust storm scheme

Spiga et al. [2013] revealed with mesoscale simulations that locally concentrated dust can create on a sub-grid scale some powerful radiatively-driven convective cells, that lift the particles very high in the atmosphere : the *rocket dust storm* phenomenon.

In GCMv6, we implement this process via a new tracer, the *stormdust*, that is distinct from the usual *background dust* tracer. At each physical time step, the model looks for the "core" of the storm, represented by the maximum stormdust mass mixing ratio (MMR) in the vertical column. It derives from then the mesh fraction within which the rocket dust storm takes place, thanks to the formula :

$$x_{\text{storm}} = \frac{q_{\text{stormdust,GCM}}}{q_{\text{storm,ref}}} \tag{2}$$

with $q_{\text{storm,ref}} = 5 \times 10^{-4}$kg/kg the reference mixing ratio of a local dust storm observed by OMEGA (Määttänen et al. [2009]). This reference MMR was derived from the opacity τ_{VIS} of the storm, which was of 10 at its maximum, and assumptions on the dust size and optical properties summed up in Section **2.3.2** of *TN_Dust_2019*. Corrected values for these assumptions, which were a bit erroneous, lead to a typical opacity of 6 instead of 10 for the dust storm we simulate in the model using $q_{\text{storm,ref}} = 5 \times 10^{-4}$kg/kg.

Furthermore, we now constrain x_{storm} between 0.01 lower bound and 0.6 upper bound. We then concentrate all the stormdust of the column on this sub-grid fraction, where its vertical maximum has approximately the same MMR as $q_{\text{storm,ref}}$. Finally, if any layer of the sub-grid fraction contains a sufficient ratio of stormdust mass over background dust ($\frac{q_{\text{stormdust}}(l)}{q_{\text{dust}}(l)} > 10^{-4}$), we trigger the rocket dust storm scheme.

Indeed, in this mesh fraction, the additional opacity induced by the presence of stormdust generates a stronger radiative heating than in the surrounding air during daytime. The radiative transfer scheme is used on this mesh fraction containing stormdust and background dust. Together with the usual radiative transfer, computed with the background dust only for the rest of the mesh, it gives a heat rate difference that makes the stormed air parcel locally rise under

the influence of buoyancy, carrying along the dust particles. A conservative Van Leer scheme (Van Leer [1977], Hourdin and Armengaud [1999]) is used to compute the vertical transport of the ascending dust.

During its ascension, some of the stormdust is detrained horizontally, and is transformed into background dust. The Figure **2** of *TN_Dust_2019*, taken from Wang et al. [2018], shows the quadratic relationship that links the vertical radiatively-induced speed of the parcel and the horizontal detrainment coefficient. In the version used for the MCD6.1, a tuned multiplicative factor of 0.02 is also put before the detrainment coefficient. When the vertical velocity becomes too low in a layer, or when there is not enough stormdust to trigger a storm, all the stormdust of the layer is detrained into background dust. This is especially the case when nights arises and no sun heats up the dust parcel anymore.

In practice, the GCM uses two ways to create stormdust tracer. The main one is by coupling the rocket dust storm and the injection schemes, as detailed in **Section 1** : the type of dust that is injected in the first layer is stormdust. This choice is relevant since the need of injection in the model generally corresponds to the apparition of a local dust storm in the scenarios. The stormdust type of the injected tracer enables the vertical advection of the particles, like during a dust storm.

On the other hand, the background dust that is present in the storm fraction of the mesh and gets partially entrained by the updraft, is thus converted into stormdust, driving the storm to higher altitudes.

3 Mountain top flows scheme

This section tackles the changes we performed in the mountain top flows parametrization (referred as *slope winds* in preceding reports), in order to make it more realistic and in line with the original idea behind it. In fact, the former scheme (see Section **3** of *TN_Dust_2019*, or Vals [2019]) used to assign to every surface mesh grid a characteristic height (or prominence) h_{mons}, computed from the local orography, that activated the top flows scheme on a sub-grid mesh fraction :

$$x_{\text{mons}} = C_{\text{mons}} \frac{h_{\text{mons}} - h_{\text{min}}}{h_{\text{max}} - h_{\text{min}}} \tag{3}$$

with h_{min} and h_{max} respectively the lowest and highest value of h_{mons} all around the globe, and C_{mons} a tunable coefficient. The Figure 1 illustrates the spatial variation of h_{mons} in the GCM.

The top flows scheme uses this mesh fraction to compute the local slope winds and to transform a given amount of near-surface background dust into *topdust* tracer, that is entrained upwards above the mountain summit. As this concentrated topdust generates a stronger radiative heating than the rest of the mesh, it then triggers a second updraft, which follows the same pattern as a rocket dust storm (see **Section 2**). If x_{mons} is large, a greater quantity of topdust will be reinjected from the boundary layer, but it will also be less concentrated as far as the radiative transfer is concerned, as the whole process operates in this fixed fraction.

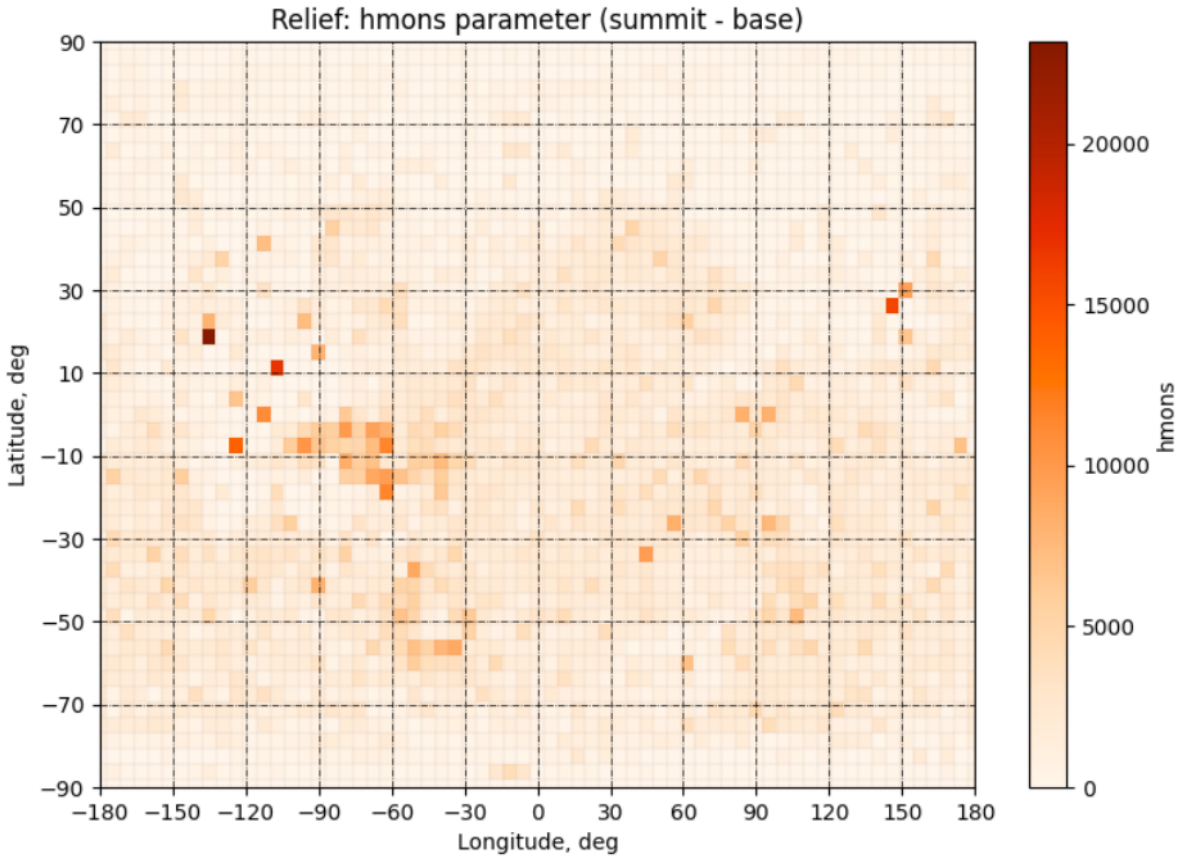

Figure 1: Registered GCM characteristic height h_{mons} (in meters) for a 64x48 horizontal resolution, computed from MOLA datum as detailed in Section **3.2** of *TN_Dust_2019*.

However this simple method had some flaws. First, since the topdust is a tracer in the model, it can be transported from the column it originated from (for instance, one with a big mountain like Olympus Mons) to adjacent meshes with flatter topography. Since each mesh has its own x_{mons}, and as the GCM tracers have no memory of their origin, the huge amount of quite spread topdust created in this Olympus Mons fraction could cross the mesh boundaries, hence arriving in a mesh with a smaller x_{mons} that artificially makes it more concentrated than it was before. This concentrated topdust generates a stronger local radiative heating that carries it to higher altitudes than what it would have reached normally.

Moreover, this scheme proved to be overgeneralizing, as it mixes up very distinct kinds of topography that may not have the accounted effect of concentrating dust above their summits. This is particularly true for cliff landscapes, which exhibit some steep and large elevations, but do not present the effect due to the converging aspect of a mountain's slopes. Hence, with the former parametrization, the model resulted in strong dust reinjection in places like the canyons of Valles Marineris, or the impact bassins of Hellas and Argyre Planitia. They were for instance responsible for an opaque feature in the clear season around 10-30°S when looking at the Column-integrated Dust Optical Depth (*CDOD*) maps, which didn't correspond to the sce-

narios used to force the dust injection (see Figure 2).

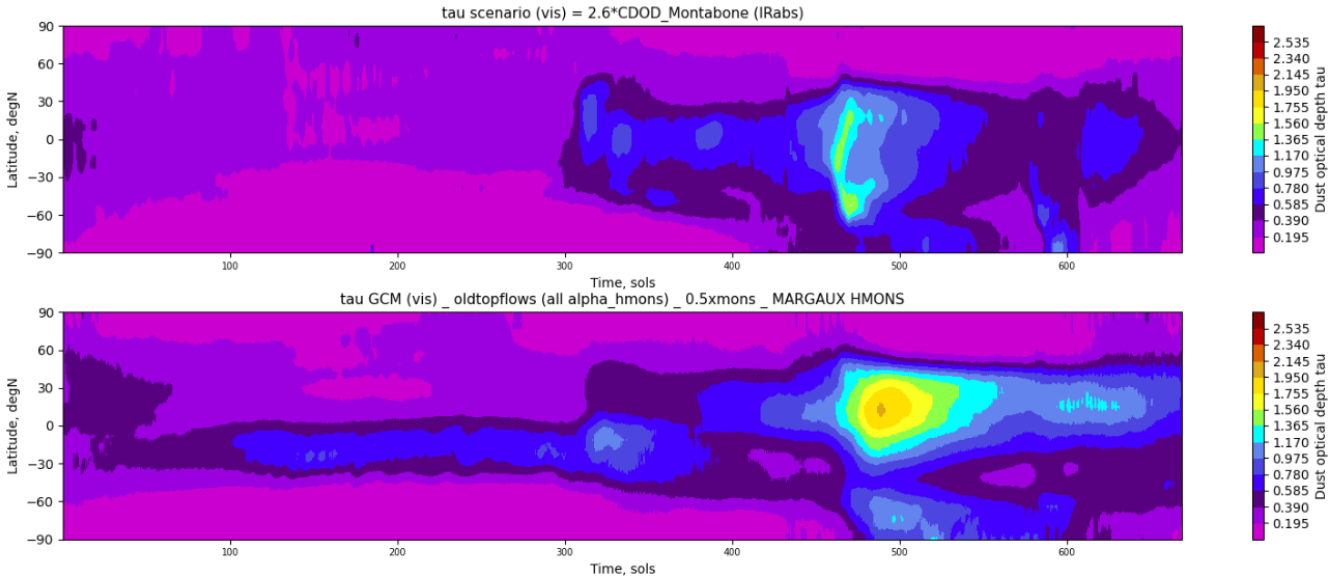

Figure 2: Time[sols]-latitude[°N] evolution over Mars Year (MY) 29 of **Top** : visible $\tau_{scenario}$ derived from Montabone et al. [2015] **Bottom** : visible τ_{GCM}, with the old top flows scheme. Every integrated optical depths are normalized to a pressure of 610Pa.

These unrealistic behaviours led us to refine the mountain top flows so that they represent well what they were originally designed for.

Revisiting this scheme began with making an inventory of the major known converging slopes on the surface of Mars. To that end, the Mars Trek portal developed by NASA JPL (Law and Day [2017]) was of great help as a way to confirm the presence of mountains. We listed a total of 19 topographic features, among which the five great volcanoes (Olympus, the three from Tharsis region and Elysium Mons) and smaller ones, but also geological massifs like Anseris Mons (Hellas Planitia) or Aeolis Mons (Gale crater). This list, non-exhaustive but still comprising the main converging slopes of the Martian surface, is detailed in Table 1 below. We chose to keep the characteristic height that was given to the grid meshes containing these mountains in the former scheme, and put all the other h_{mons} of the planet to zero, preventing the top flows to activate there. This also implies detraining the topdust into background dust as soon as it leaves the columns containing mountains, which may not be that realistic but still seems a better solution. An improvement of this in future versions could be done via tagging the topdust tracers to keep track of their original mesh fraction, in the same manner as Bertrand et al. [2020], or by changing topdust into stormdust since the two processes are very similar after the topdust has been entrained by the slope winds.

Since we restrict the top flows scheme to these mountains only, we decide not to dampen their effect too much by keeping the fraction x_{mons} as a linear function of h_{mons}, with a C_{mons} coefficient of 0.5.

Mountain name	**Location (longitude ; latitude)**	**GCM mesh h_{mons} (summit-base)**
Olympus Mons	-134.0°E ; 18.4°N	23.2km
Ascraeus Mons	-104.5°E ; 11.8°N	16.8km
Elysium Mons	146.9°E ; 24.8°N	15.9km
Arsia Mons	-121.1°E ; -8.4°N	14.0km
Pavonis Mons	-113.4°E ; -0.8°N	11.1km
Hecates Tholus	150.2°E ; 31.8°N	9.4km
Tharsis Tholus	-90.8°E ; 13.4°N	8.0km
Ceraunius Tholus	-97.4°E ; 24.0°N	7.4km
Alba Mons	-109.6°E ; 40.4°N	7.2km
Apollinaris Mons	174.4°E ; -9.3°N	7.0km
Albor Tholus	150.4°E ; 18.8°N	6.6km
Biblis Tholus	-124.6°E ; 2.6°N	6.6km
Anseris Mons	86.6°E ; -29.8°N	5.6km
Ulysses Tholus	-121.6°E ; 2.9°N	6.6km *(merged with Biblis Tholus in the 64x48 GCM resolution)*
Aeolis Mons	137.8°E ; -5.4°N	4.3km
Euripus Mons	105.0°E ; -44.8°N	4.1km
Hadriacus Mons	91.8°E ; -32.1°N	2.4km
Tyrrhenus Mons	106.5°E ; -21.1°N	1.5km
Uranius Mons	-92.2°E ; 26.8°N	1.5km

Table 1: List of inventoried mountains in the GCM new top flows scheme, and the h_{mons} parameter of their corresponding grid mesh in the usual 64x48 horizontal resolution.

These changes in the modeling of mountain top flows result in a much more reasonable optical depth, as can be seen on Figure 3. On the dust vertical profile, highlighted by Figure 4, the detached layers present before are now shallower in the clear season, even compared to MCS, but the new top flows still enable some dust to reach mid altitudes (pressures below 100Pa). In the second half of the year, the effect of the changes are less pronounced because of the prominence of the rocket dust storms, apart from the period after the solar longitude L_S=300° that sees a decrease in amplitude (but not in altitude) of the detached layers, even compared to the simulation without top flows. Eventually, a peak of IR density-scaled opacity around L_S 240° is much stronger in every simulations than MCS observations. This storm is also noticeable on VIS CDOD maps (Figure 3), where this time the GCM seems to have less dust than in the observations. This discrepancy is a recurrent paradox we found when trying to validate the GCMv6, and the next section tackles the optical properties of the dust aerosol to partially solve this issue.

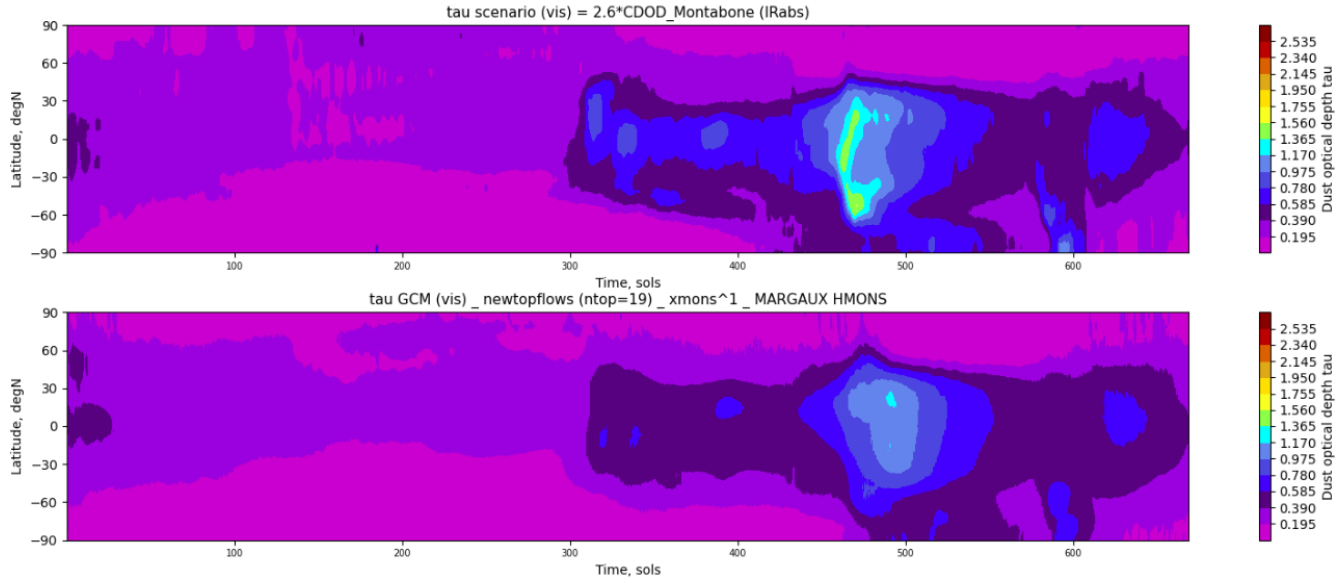

Figure 3: Time[sols]-latitude[°N] evolution over MY29 of **Top** : visible $\tau_{scenario}$ derived from Montabone et al. [2015] **Bottom** : visible τ_{GCM}, with the new top flows scheme. Every integrated optical depths are normalized to a pressure of 610Pa.

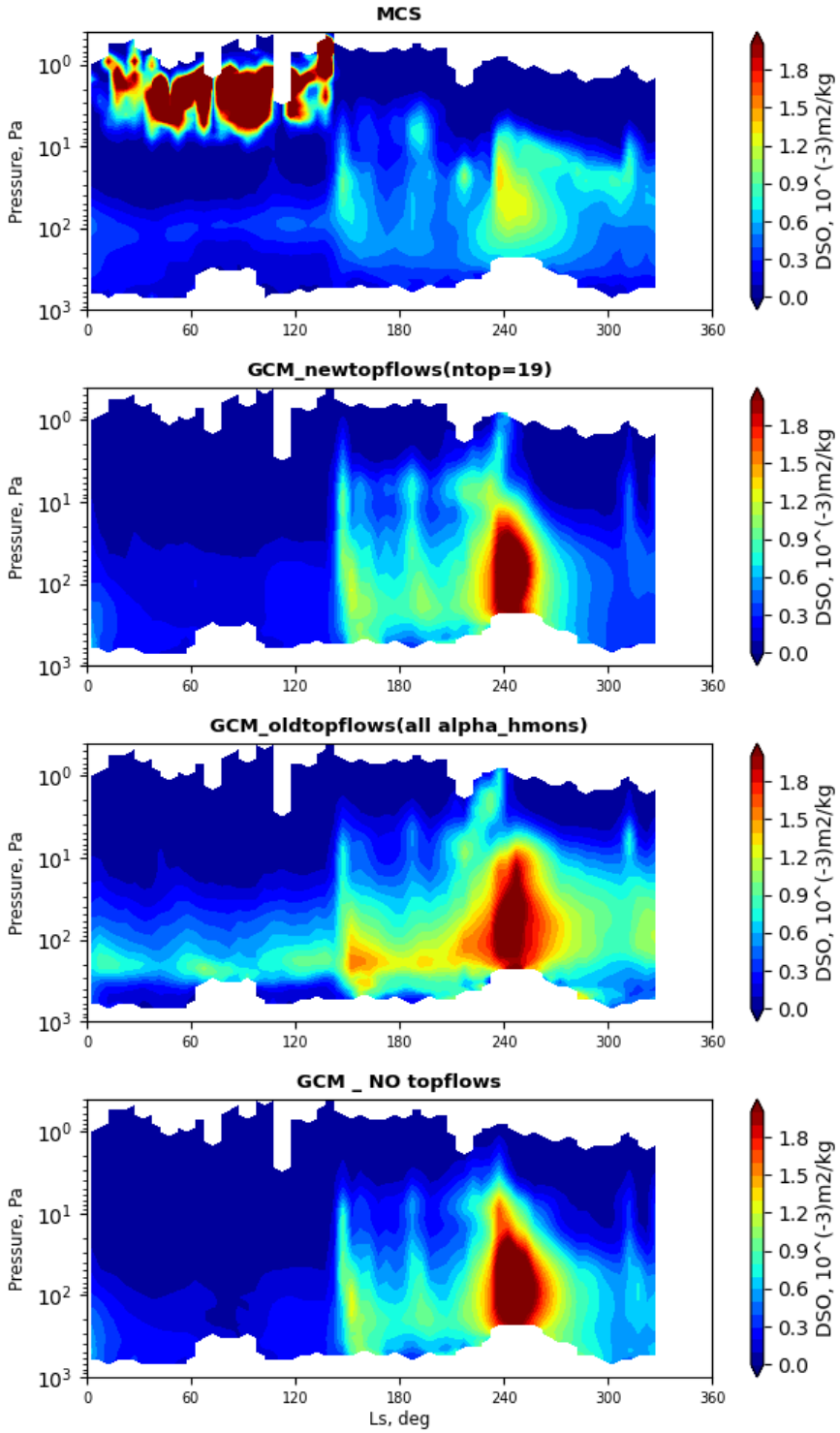

Figure 4: Nighttime dust Density-Scaled Opacity at 21.6µm from MCS and several GCM simulations - Zonal & meridional average in latitude band of [30°S;30°N] - MY29. **Top to bottom** : MCS ; GCMv6 with new top flows scheme ; GCMv6 with old top flows scheme ; GCMv6 without top flows. *Note: the saturated high-altitude opacity in MCS retrievals (L_S=0-150°, P<10Pa) are DSO artifacts and should not be considered when trying to assess the match with the model.*

4 Optical properties and conversion between wavelengths

As explained in **Section 1**, in order to simulate a realistic Martian dust cycle, the GCM is forced by CDOD scenarios. These scenarios have been built by Montabone et al. [2015],Montabone et al. [2020] based on the observations from multiple instruments orbiting the planet. The major supply of opacity measurements used in the latest Martian years is from *Mars Climate Sounder*, a mid- and far-infrared thermal emission radiometer performing nadir and limb soundings of the atmosphere (Kleinböhl et al. [2009]). This instrument measures dust absorption opacity profiles at the IR wavelength of 21.6µm, which is then converted into extinction opacity in the retrievals thanks to the relation $\tau_{ext} = \frac{\tau_{abs}}{(1-\omega)}$. ω represents the single scattering albedo of the dust particle, assumed to be 0.0550 by Kleinböhl et al. [2011] at this wavelength.

To build the CDOD scenarios, these extinction opacity profiles at 21.6µm are then extrapolated down to the surface, and Montabone et al. [2015] infer an IR absorption optical depth at 9.3µm using a ratio of 2.7 from the opacity at 21.6µm.

Finally, in the model, we compute a visible (0.67µm) extinction CDOD from the absorption 9.3µm scenario using a coefficient of 2.6 mentioned in Montabone et al. [2015], and we make the model visible CDOD follow the scenario by injecting each day a dust amount corresponding to the difference between the two. Using these hypotheses, we found that the model exhibits paradoxical behaviours, as the visible CDOD remains near below the target scenario, while the comparison to the direct MCS 21.6µm extinction opacity suggests a strong overestimation of the simulated atmospheric dust quantity.

The transition from the MCS measurements in the mid-far infrared to the visible CDOD scenario as it is used in the GCM requires to go through these two conversions, which carry some hypotheses on the particle distribution. For the conversion $\tau_{abs,9.3\mu m} \rightarrow \tau_{ext,0.67\mu m}$, Montabone et al. [2015] suppose a r_{eff}= 1.5-2µm which gives them a coefficient of 2.6. In theory :

$$\frac{\tau_{ext,0.67\mu m}}{\tau_{abs,9.3\mu m}} = \frac{Q_{ext,0.67\mu m}}{Q_{ext,9.3\mu m} * (1 - \omega_{9.3\mu m})} \tag{4}$$

with τ_{ext} and τ_{abs} the extinction and absorption opacities [1/km] at given wavelengths. The extinction efficiencies Q_{ext} and the single scattering albedo ω are the optical properties of the dust particles, which depend on the size distribution. In the GCM, the size of the dust particles present in the atmosphere is assumed to follow a log-normal distribution, that can be fully described by the tuple of its effective radius r_{eff} and variance ν_{eff}. We use tabulated optical properties computed from a T-Matrix code for a large range of effective radii, at a very small variance that is almost representative of one isolated particle's optical properties (Madeleine et al. [2011]). We can then compute the properties for multiple variances by convolution methods and simulate different size distributions.

On Figure 5, we plot the computed value of this theoretical coefficient for multiple variance assumptions, as well as the value given by Montabone et al. [2015]. This shows that the coefficient value used to convert the scenarios into VIS CDOD is highly dependent on the particle size r_{eff}. We can thus question the reliability of the 2.6 value to represent the dust distribution at every time of the year, everywhere around the globe.

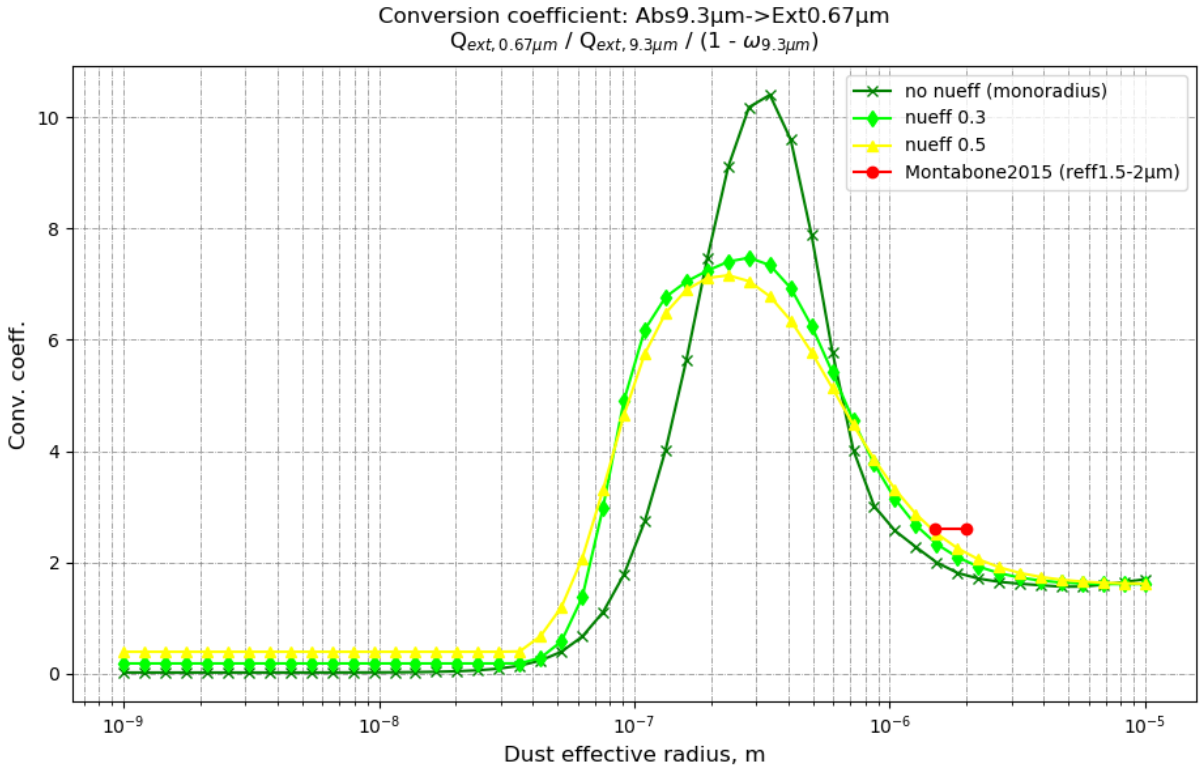

Figure 5: Conversion coefficient from dust absorption at 9.3µm to extinction at 0.67µm as a function of effective radius, computed from T-matrix generated tables of optical properties used in the GCM. The dark green curve is computed with no dust distribution variance (isolated particles properties), the lime green and yellow ones with ν_{eff} = 0.3 and 0.5 respectively. The red points are values reported from Montabone et al. [2015].

In the model, we work at a fixed dust effective variance of 0.5, while the effective radius in a grid mesh is given by the two transported dust moments, the mass mixing ratio q [$\text{kg}_{\text{dust}}/\text{kg}_{\text{air}}$] and the number mixing ratio N [$1/\text{kg}_{\text{air}}$], with the relation :

$$r_{\text{eff}} = \left(\frac{3}{4}\frac{q}{\pi\rho_{\text{dust}}N}\right)^{1/3}(1+\nu_{\text{eff}}) \tag{5}$$

Hence, we decided to implement a refined conversion of the 9.3µm absorption CDOD scenarios into visible extinction by taking into account the modeled r_{eff}. This is done while loading the scenario once per sol, as we compute the *IR to VIS ratio* as the ratio of the model CDOD at both wavelengths.

By analysing the evolution of this ratio on Figure 6 while keeping Figure 5 in mind, one can observe a net difference between the clear season, where only fine dust grains ($r_{\text{eff}} \approx 1\mu\text{m}$) stay in the atmosphere leading to an increased IR to VIS ratio, and the dusty season when the storms can lift larger particles ($r_{\text{eff}} \approx 2\mu\text{m}$), which deviate the dust size distribution towards lower conversion coefficients than before. In the polar nights finally, the coefficient follows Figure 5

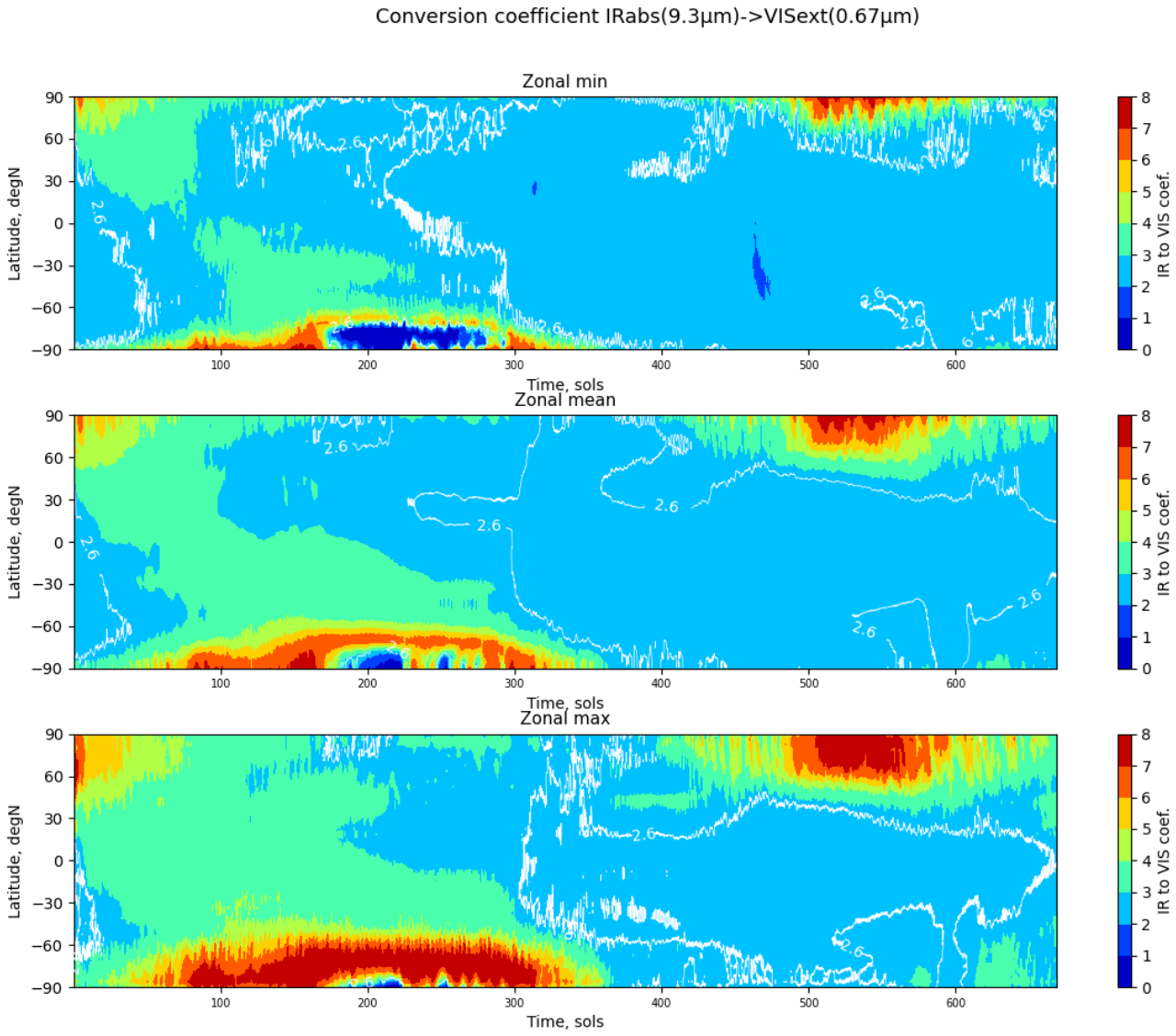

Figure 6: Evolution maps (time-latitude) of the IR to VIS ratio predicted by the GCM over MY29. **Top** : zonal minimum. **Middle** : zonal average. **Bottom** : zonal maximum. The white contours delimit the plot areas above and below the former constant value of 2.6.

as we go poleward, witnessing a decreasing particle size in these regions and times.

Therefore, it appears that taking into account this diversity of dust sizes in the conversion coefficient for the scenario results in a lower forcing during the second half of the year, making the GCM inject less dust than before (Figure 7) and get closer to MCS opacity profiles (Figure 8). On the other hand, by increasing the forcing in the first part of the year, it favors the persistence of mid-altitude (approx. 100Pa, or 20-30km) dust that can form dust detached layers.

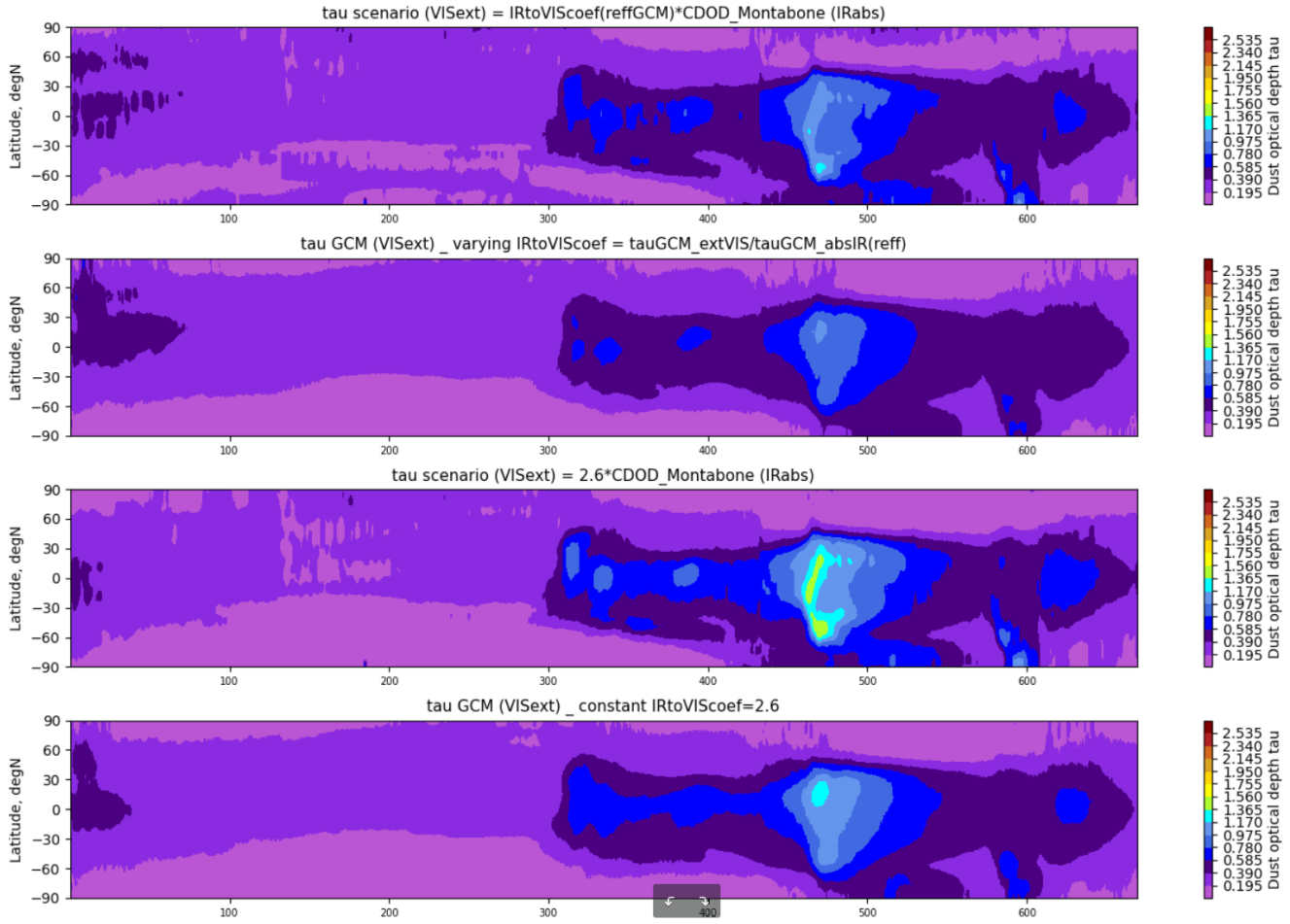

Figure 7: Time[sols]-latitude[°N] evolution maps over MY29 of visible $\tau_{scenario}$ and τ_{GCM} with and without IR to VIS ratio in the GCM. **Top 2 plots** : The visible CDOD scenario forcing, computed from IR (9.3µm absorption) scenario and the varying IR to VIS coefficient, and the correspondingly driven visible CDOD from the GCM. **Bottom 2 plots** : same plots as above but with the former constant value of 2.6. Every integrated optical depths are normalized to a pressure of 610Pa.

Furthermore, the dust opacity plays a big role on the atmospheric thermal structure, via the radiative transfer. By decreasing the amount of dust injected during the dusty season, the varying IR to VIS ratio also has the effect of reducing the hot bias present in GCMv6 at this time, down by 5K in some cases (around L_S 240°,100Pa), as shown on Figure 9.

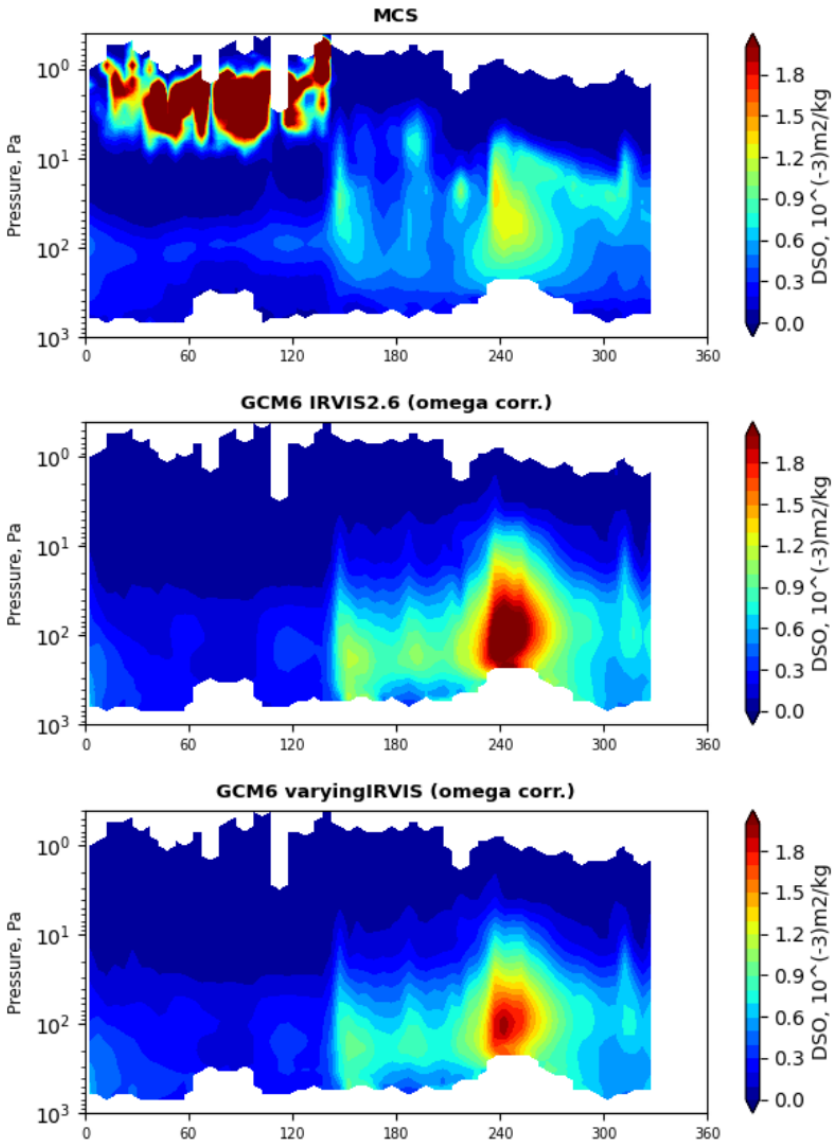

Figure 8: Nighttime dust Density-Scaled Opacity at 21.6µm from MCS and several GCM simulations - Zonal average in tropics (30°S-30°N) - MY29. **Top to bottom** : MCS ; GCMv6 with constant 2.6 conversion coefficient for the scenario ; GCMv6 with the new r_{eff}-dependent conversion coefficient for the scenario.

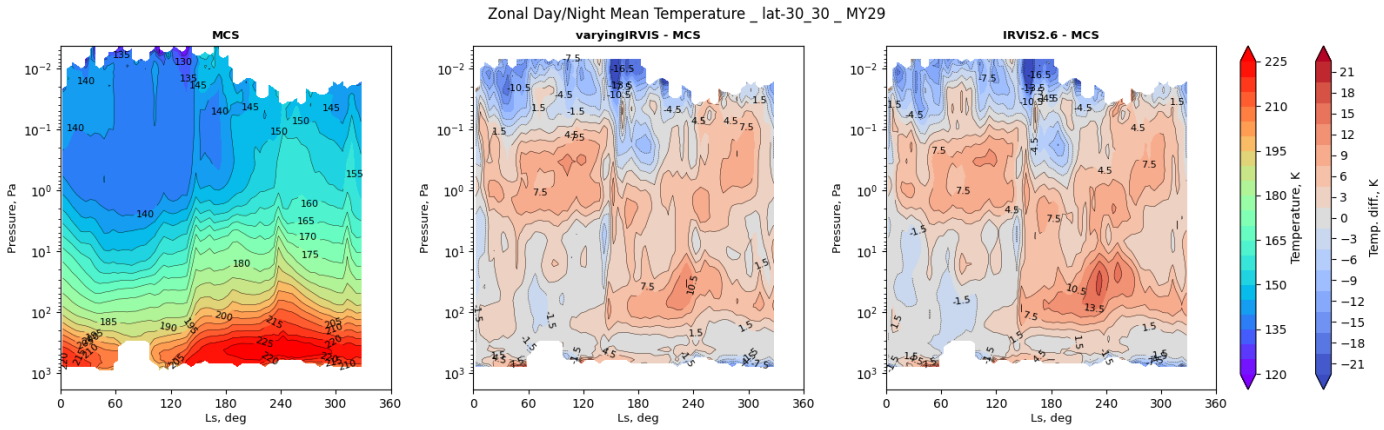

Figure 9: Temperature profile evolution over MY29, from MCS and GCM simulations - Zonal and diurnal average in tropics (30°S-30°N). **Left to right** : MCS absolute temperature ; Temperature difference between GCMv6 with the new r_{eff}-dependent conversion coefficient and MCS ; Temperature difference between GCMv6 with constant 2.6 conversion coefficient and MCS.

5 Dust radiative adjustment

Unlike GCMv5, the GCMv6 does not match perfectly the VIS CDOD scenario as it lets the dust freely evolve without renormalization. Here we add a little safeguard in this new dust cycle, so that a GCM dust column that is far from the scenario does not impact the atmospheric thermal structure too much.

To do so, we implemented a new dust scaling mode that is less constraining than the GCMv5 full "tauscaling" renormalization computed at every timestep, but uses the same principle. At 14h locally, we evaluate the target dust scenario opacity for the next sol and compute a scaling factor :

$$dust\_rad\_adjust(sol, 14h) = \frac{\tau_{\text{pref,scenario}}(sol+1, 14h)}{\tau_{\text{pref,gcm}}(sol, 14h)} \tag{6}$$

In order to preserve the dust diurnal cycle and prevent jumps of *dust_rad_adjust* at 14h, the coefficient is smoothed by linear interpolation, between the current sol at 14h and the next sol at 14h. This scaling factor is then applied to all the dust types opacities (background dust, stormdust and topdust) when computing their radiative effect.

In practice, this scaling factor remains quite close to 1 in average, but can locally strongly diverge from unity. Thus, we decide to put an upper limit to *dust_rad_adjust*, in order to prevent local spikes that arise in the model, mainly in polar nights, and could potentially disrupt the temperature there. Indeed,

- the polar nights are the least constrained places in the dust observations, and are mainly extrapolated by kriging from lower latitudes in the CDOD scenarios (Montabone et al. [2015]) ;
- the polar nights have the lowest dust optical depths. This is due to the scavenging of the atmospheric dust by the water and CO_2 clouds (see **Section 6**), and the absence of the solar radiation that generates elsewhere dust-lifting convection and turbulence. Thus, any occasional increase of the dust amount there is accentuated comparatively to the background level ;
- the polar regions are the places with the most diurnal and day-to-day variability, because of the strong effect of the baroclinic waves at these latitudes, which can sporadically bring some dust from lower latitudes. This implies that the *dust_rad_adjust* scaling factor, evaluated at 14h and simply interpolated from day to day, can get strongly unrealistic a few hours later and input the radiative transfer with huge optical depths.

Another terrain where this upper limit matters is the big volcanoes. The variability of the background dust is indeed quite high in these meshes, because a lot of it is transformed into topdust during daytime. This topdust should not be accounted for in the background radiative transfer to compute the mesh temperature, since any extra heating due to its presence is converted into upward motion.

Therefore, this upper limit, set to a ratio of 5 in the model, ensures to keep realistically low corrected CDODs in the polar nights and above the mountains, while not affecting the rest of the planet where the *dust_rad_adjust* ratio generally lies around unity (see Figure 10).

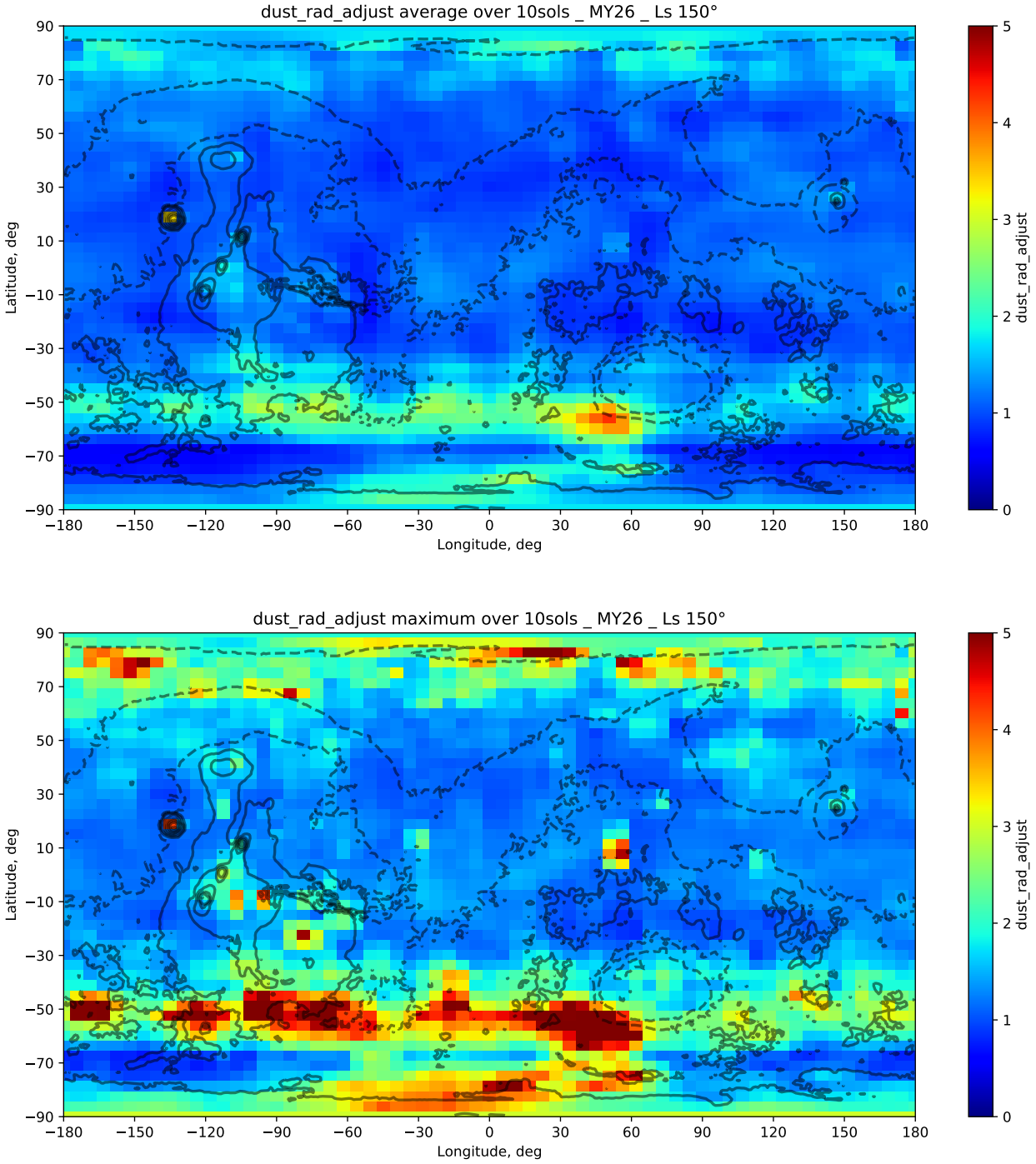

Figure 10: Map of the *dust_rad_adjust* scaling factor from a GCMv6 simulation, around L_S 150° of MY26. The black contours represent the topography. **Top** : average *dust_rad_adjust* factor over 10 sols. **Bottom** : maximum *dust_rad_adjust* factor over 10 sols.

6 Scavenging of aerosols by the CO_2 snow

Now that the dust is not normalized to the scenario CDOD anymore, one discrepancy that appears is the presence of airborne dust in the polar nights, especially the Northern one (during the dusty season). Even though no dust injection is done in meshes covered by CO_2 ice caps, the transport of aerosols from lower latitudes increases the GCM polar dust optical depth to levels that are not consistent with the scenarios.

This overestimation was partially solved by taking into account the scavenging of the aerosols by CO_2 ice clouds. In the model, atmospheric CO_2 condensation is accounted for since Forget et al. [1998], but not its effect on aerosols. Indeed, these particles serve as nucleii for heterogenous condensation of the CO_2 (Määttänen et al. [2005]), and are scavenged from the atmosphere by CO_2 snow precipitation. We implemented a new parametrization to represent this process, where we assume a proportional relationship between the mass of aerosol trapped in CO_2 snow and its local atmospheric concentration, thus introducing the scavenging ratio:

$$\mathcal{R}_{\text{scav}} = \frac{q_{\text{aerosol in CO}_2\text{ snow}}}{q_{\text{aerosol in air}}} \tag{7}$$

Due to a variety of mechanisms (heterogeneous nucleation, radiative cooling of the aerosols, coalescence, collision), $\mathcal{R}_{\text{scav}}$ should be higher than 1, but is not well constrained by observations, leaving it as a tunable parameter for the model. We use the same value of $\mathcal{R}_{\text{scav}}$=20 for dust and water ice aerosols, which are both scavenged by CO_2 snow.

This parametrization is extensively detailed in the companion *Deliverable Document D2 - Part 2 : Improving the Water Cycle*, since its impact is of first order on the polar water clouds and the water cycle as a whole. Sensitivity studies on $\mathcal{R}_{\text{scav}}$ hence led to make a compromise between a good removal of dust and keeping a sufficient amount of water ice particles in the polar night.

Eventually, the CO_2 condensation scheme, including the scavenging of aerosols, is due to evolve in the future versions thanks to the implementation of the CO_2 clouds microphysics in the PCM, which will introduce CO_2 ice particles and their condensation nucleii (dust, water ice, meteoritic particles) as tracers, which can be transported and sedimented by the model. Updates on this scheme are presented in the *Deliverable Document D2 - Part 3 : Modeling the CO_2 Microphysics*.

7 Results and discussion

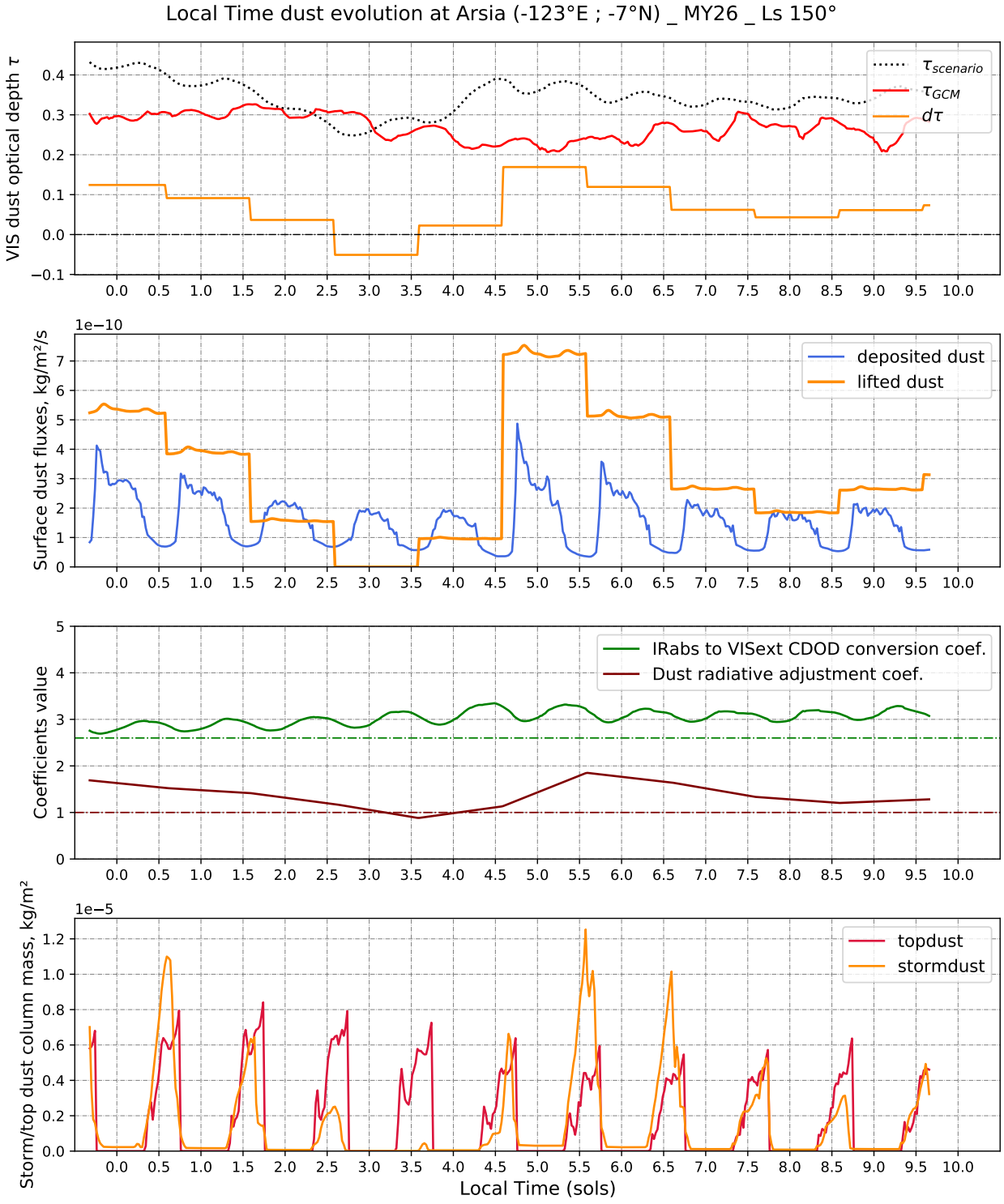

Figure 11: Time evolution over 10 sols of the GCMv6 dust cycle variables, at Arsia Mons, around L_S 150° of MY26. The x-axis is the Local True Solar Time (in sols) at the longitude of Arsia Mons GCM mesh : $LTST = LTST(lon\ 0°E) + \frac{-123.75°E}{360°}$ where x.5 sol corresponds to local noon.
1st row : Visible extinction CDODs of the scenario (black dotted curve) and the GCM (red solid curve). The orange solid line displays the difference $\Delta\tau = \tau_{\text{pref,scenario}} - \tau_{\text{pref,gcm}}$ computed everyday at 14h ($\approx$ 0.583sol) and used for the injection. These CDODs are normalized to a pressure of 610Pa.
2nd row : Surface flux [kg/m²/s] of lifted stormdust by the injection scheme (orange curve). For reference, the blue curve shows the background dust deposition flux at the same time.
3rd row : In green, the *IRtoVISratio* (solid curve) used to convert the IRabs scenario into VISext CDOD, with the dashed line denoting the old value of 2.6. In dark red, the *dust_rad_adjust* scaling factor (solid curve), with the ratio of 1 displayed by the dashed line for reference.
4th row : Column-integrated mass [kg/m²] of atmospheric topdust (red curve) and stormdust (orange curve).

Figure 11 compiles the different aspects of the GCMv6 dust cycle that have been tackled in this report, here focusing on Arsia Mons grid mesh at the end of the Northern Summer of MY26.

At the beginning of the simulation, $\tau_{\text{pref,gcm}}$ lies below the next sol target $\tau_{\text{pref,scenario}}$ (1st row), inducing a *dust_rad_adjust* scaling factor (3rd row) higher than 1 for the computation of the radiative transfer. The positive $\Delta\tau$ (1st row) triggers the injection of stormdust (2nd row). This stormdust remains in stable low quantity in the column at night (4th row), as the constant injection rate is continually compensated by the detrainment into background dust, which partially sediments to the surface (2nd row).

When morning arises, the sun heating delays the detrainment of stormdust, which soars up and entrains background dust with it, reaching its peak in the early afternoon (4th row). This injection of big dust particles ($r_{\text{eff,lift}}$=3µm) changes the dust size distribution and decreases the *IRtoVISratio* of the column optical depth (3rd row), while at night, only the smaller particles stay in the atmosphere and increase the conversion coefficient. These variations of *IRtoVISratio* echo on the VIS scenario CDOD, which exhibits a diurnal cycle (1st row) (while the IR CDOD from Montabone et al. [2015] only has one value per sol).

The fact that $\tau_{\text{pref,gcm}}$ (computed on background dust only) doesn't evolve much (1st row) despite a stronger injection than the deposition rate (2nd row) suggests a local net loss of background dust due to transport to adjacent columns. This is especially the case when the dust gets high in the atmosphere, as the horizontal winds become stronger far from the surface. At Arsia Mons, two mechanisms make the dust rise : the rocket dust storms, whose intensity strongly depends on the dust scenarios ; and the mountain top flows, which peak slightly later in the afternoon (4th row), and show a lower day-to-day variability.

Both processes also have a seasonal evolution (not visible with these plots). The rocket dust storms become predominant during the dusty season (2nd half of the year) when the scenarios feature big dust storms, whereas the top flows intensity follow the meridional drift of the subsolar point, which provides greater energy to the slope winds. At L_S 150° of MY26, the dusty season has not yet begun, although some small dust storms are seen in the Southern Hemisphere

and lead to a moderate dust loading around Arsia ($\tau_{\text{pref,scenario}} \approx 0.35$). Meanwhile, the subsolar point is still in the Northern Hemisphere, so Arsia's top flows are just emerging. These conditions occasion similar amounts of stormdust and topdust to be injected above Arsia at this time of the year (4th row).

To further comment on the VIS CDOD agreement of GCMv6, the $\tau_{\text{pref,gcm}}$ displayed on 1st row of Figure 11 is actually characteristic of the general behaviour of the model, which is able to simulate a real diurnal evolution. On the other hand, despite following quite reasonably the scenario tendencies, there exists a systematic small negative bias in the model VIS CDOD compared to these observations.

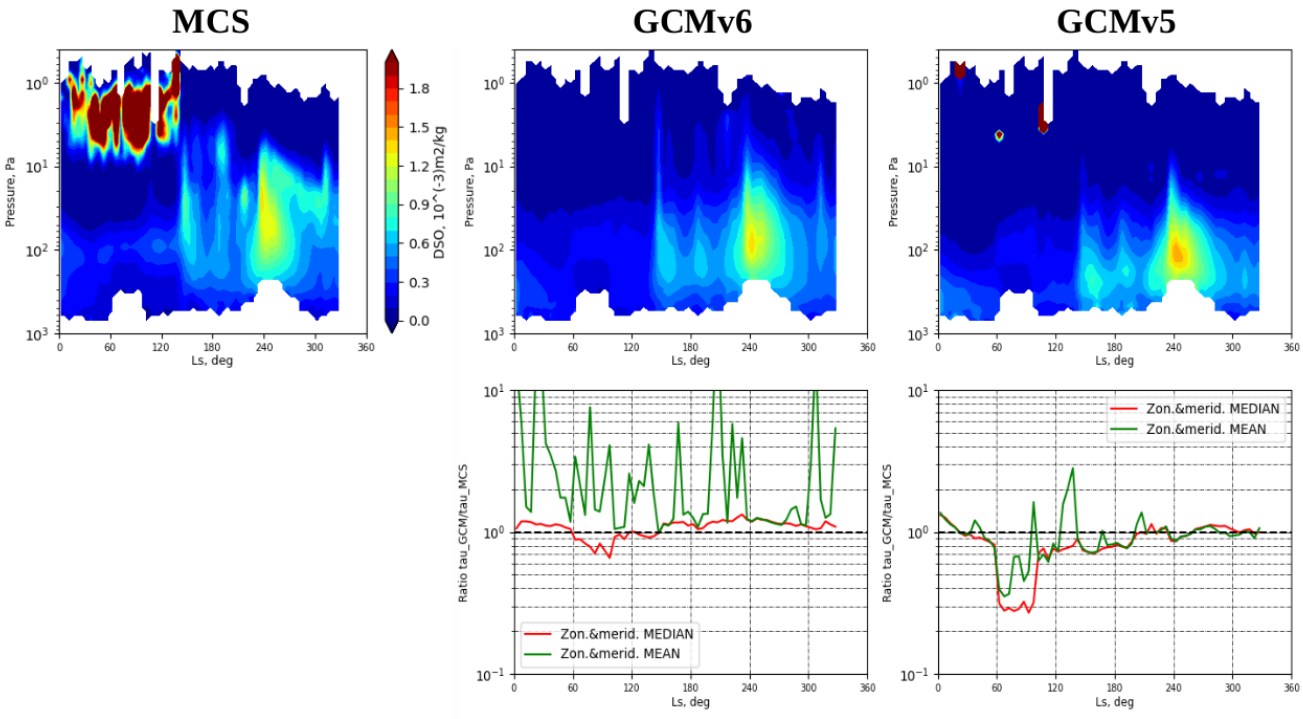

Figure 12: Nighttime dust 21.6µm extinction Density-Scaled Opacity over MY29, from MCS and GCM simulations - Zonal average in tropics (30°S-30°N). **Top row, left to right** : MCS DSO ; GCMv6 DSO ; GCMv5 DSO. The GCM opacities are renormalized to the MCS optical depth integrated over its field of view, in order to highlight the vertical distribution. **Bottom row, left to right** : Renormalization ratios τ_{GCM}/τ_{MCS} for GCMv6 and GCMv5 respectively. The red curve represents the zonal tropical median, while the green one stands for the average. The black dashed line emphasizes a ratio of unity. *Note: the saturated high-altitude opacity in MCS retrievals (L_S=0-150°, P<10Pa) are DSO artifacts and should not be considered when trying to assess the match with the model. These strong DSOs do not affect the column-integrated τ_{MCS} because of the very low density at these altitudes.*

We can also compare the GCMv6 dust cycle to a GCMv5 simulation. Figure 12 illustrates the agreement of MY29 simulations to the MCS nighttime opacity, in terms of profile shape on the one hand, and of absolute integrated optical depth on the other hand. Indeed, these figures' top rows present the GCM dust Density-Scaled Opacity profile normalized by the local column-integrated optical depth of the MCS binned profile. To do so, the GCM data are processed through our MCS observation simulator, which interpolates GCM files at MCS observation locations and exact local times[5] and reproduces the binning by 5° of L_S of the MCS files. The simulator also computes locally the column-integrated optical depth of both MCS and interpolated GCM profiles, and outputs the ratio :

$$\frac{\tau_{GCM}}{\tau_{MCS}} = \frac{\sum_{l=l_{MCS,bot}}^{l_{MCS,top}} [\partial_z \tau_{GCMinterp.}(l)\ \Delta P_{lev,MCS}(l)\ /\ g\rho_{MCS}(l)]}{\sum_{l=l_{MCS,bot}}^{l_{MCS,top}} [\partial_z \tau_{MCS}(l)\ \Delta P_{lev,MCS}(l)\ /\ g\rho_{MCS}(l)]} \tag{8}$$

with $P_{lev,MCS}(l)$ the mid-altitude pressure between two MCS pressure grid points $P_{lev,MCS}(l) = \sqrt{P_{MCS}(l-1)P_{MCS}(l)}$; and $\rho_{MCS}(l) = \frac{P_{MCS}(l)}{r_{atm}T_{MCS}(l)}$ the atmospheric density derived from MCS temperature retrievals.

The dust vertical profile from GCMv6 is shifted to higher altitudes than in GCMv5, with an annual average tropical maximum around 20km, and clear detached layers in the dusty season. Considering the τ ratios, the median curves (red) indicate that the GCMv6 simulation achieve to lift satisfying amounts of dust at the levels comprised in MCS field of view. This is especially true at the time of the aphelion cloud belt (L_S 60°-100°), when the observations are limited to higher altitudes than usual because of the thick tropical water clouds, as GCMv6 greatly improves the agreement with MCS compared to GCMv5 dust that is confined near the surface. We can notice several inconsistencies though.

First, both GCM simulations, even the GCMv5 one, exhibit this *detached layer*-like shape between L_S 60° and 100° once passed through the observation simulator and renormalized by MCS column. This could point toward an observational bias, especially as this shape disappears in the GCMv5 simulation as soon as we look directly at the opacity profiles interpolated at 3am for instance (see Figure 13).

Second, GCMv6 fails to exhibit a real "detached" feature in the clear season, and rather looks like a vertically extended well-mixed profile, implying that the mountain top flows, which enable this vertical extension, are not sufficient as things stand to produce and sustain the detached layers seen by MCS. The potential contribution of near-polar dust storms, triggered by the strong katabatic winds at the cap edge, and not always detected by the observations used for the scenarios, will be a subject of study in the next versions of the PCM.

Third, in the dusty season, simulated detached layers reach lower altitudes than what is seen by MCS. Studies to better assess the dust lifting timing for the injection could enable to have more concentrated rocket dust storms that go higher, but this can not be done without looking at the same time to reduce the dust infrared opacity to match the MCS dust retrievals. Indeed, the GCMv6 median dust optical depth integrated along MCS field of view, in 21.9µm

[5]Former method used to look at GCM data at 3am/3pm, which are the Mean Solar Local Times of the MCS observations at the equator, but the true local time can strongly vary with latitude and throughout the year.

extinction, gets higher than the observations in the dusty season ($\tau_{GCM}/\tau_{MCS} \approx 1.2$). This point contradicts at first with the fact that the GCM VIS full-column optical depth is lower than the CDOD scenarios, yet built from MCS data. Several factors could explain these paradoxical diagnoses : the denser near-surface layers, which have the strongest weight in the CDOD, are not seen by MCS limb observations, and extrapolating in the scenarios requires assuming a well-mixed profile below the lowest observation (Montabone et al. [2015]) ; the conversion coefficient from MCS 21.9µm extinction to the scenarios 9.3µm absorption is also theoretically dependent on the dust effective size, like the *IRtoVISratio*, although considered constant by Montabone et al. [2015] ; finally, the dust effective size and the particle shape could be badly represented in the model and lead to wrong VIS to 21.9µm extinction ratios. GCMv6 simulation of MY25 extreme dust event and its decay phase especially hints at a too slow sedimentation, which is one of the main processes affecting the modeled atmospheric dust size. This is also supported by the average ratio τ_{GCM}/τ_{MCS} (green curve on Figure 12, bottom row, left) that can become far greater than unity in between the storms and indicates the presence of some opacity profiles that highly depart from MCS in the considered dataset.

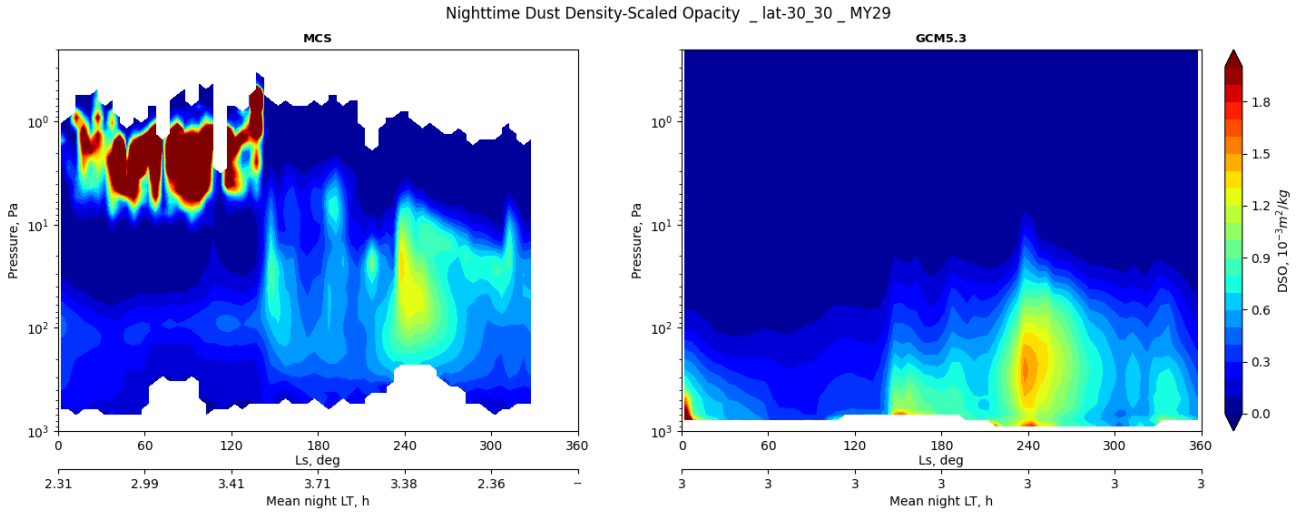

Figure 13: Nighttime dust 21.6µm extinction Density-Scaled Opacity over MY29 from : **left** MCS, and **right** GCMv5 simulation just interpolated at 3am everywhere. Zonal average in tropics (30°S-30°N). The average local time of the MCS observation corresponding to the L_S labels is also written for comparison.

On Figure 14 we examine the impacts the new dust cycle has on the mean atmospheric temperature.

During the clear season first (L_S=0°-150° in MY29), the dust cycle-related changes presented in this report do have an impact on the mid-altitude temperature (see for example Figure 9 in Section 4), and the vertically extended dust profile mentioned above certainly contributes in the warming of the atmosphere. However, the improvements in the water ice clouds representation (see *Deliverable Document D2 - Part 2 : Improving the Water Cycle*), which are strong

drivers of the thermal structure at this time of the year, also explains our better results during this season, compared to GCMv5.

We can also note that the changes done in GCMv6 with regard to GCMv5 (improved dust and water cycles, non-orographic gravity waves) have very little influence at this season on the high-altitude (P < 2Pa) temperature bias, which must be due to other processes.

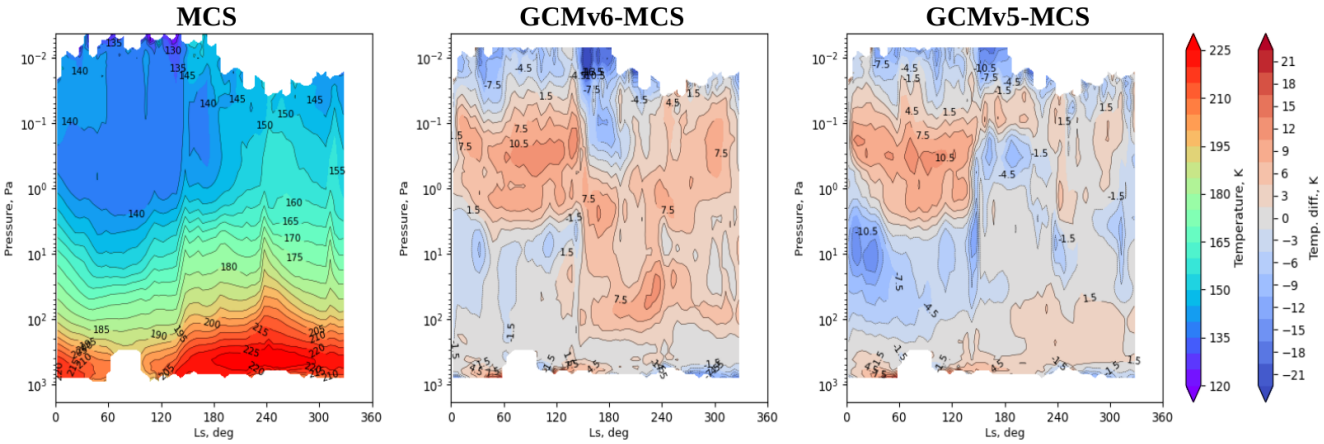

Figure 14: Temperature profile over MY29, from MCS and GCM simulations - Zonal and diurnal average in tropics (30°S-30°N). **Left to right** : MCS absolute temperature ; Temperature difference between GCMv6 and MCS ; Temperature difference between GCMv5 and MCS.

Later, the dusty season displays a mid-altitude (200Pa-10Pa, or approximately a 10-40km range) hot bias, which peaks above 10K during the big A-storm at L_S 240° of MY29. This adds to the discrepancy between the VIS CDOD and the 21.6µm extinction opacity profiles of the GCM. Indeed, the VIS CDOD, that lies slightly below the scenario, would normally be corrected via *dust_rad_adjust* and involve similar temperatures than the observations (since dust heats its environment mainly by absorbing the visible sunlight during the day). However, the fact that temperatures are hotter than MCS during the dusty season would suggest a too strong radiative effect of the dust aerosol, either because of its mass amount (which is supported by the stronger 21.9µm extinction, almost independent of the dust size), or its optical properties (strongly related to its size distribution in the visible), or because of both. Marginally increasing the visible dust albedo in the range of its uncertainty (see Figure 8 of Wolff et al. [2009]) to better reflect sunlight cools the atmosphere only by a few kelvins where the dust is present, which fails to compensate for this hot bias. We will however closely follow the latest progresses made in the characterization of the dust optical properties, as some laboratory studies (Martikainen et al. [2022]) have recently questioned the reference tables from Wolff et al. [2009]. Besides, further validating and improving the dust effective size in future versions of the PCM should result in different opacities and thermal effect.

Closer to the surface (P > 200Pa), the temperature is slightly more consistent with the observations than GCMv5, because the mid-altitude airborne dust decreases the amount of the incident visible radiation in the lower layers.

On the opposite, the low mesosphere (P < 10Pa) also seems impacted by the presence of the aerosol particles. The hot bias linked to this high dust loading could be reduced in future versions of the PCM by implementing the non-local thermal equilibrium between dust and gas above 40km, which has been brought in light by Goldenson et al. [2008] and recently tested in 1-D radiative-convective and 3-D dynamical models by Haberle et al. [2022]. The latter suggests that even though the NLTE only occurs above 40km, it can affect the general circulation and thus indirectly change the thermal structure even below 40km. The temperature changes were however quite small in their simulations, but supposed a fixed dust profile that mostly confines dust below 50km, which differs from our model.

Finally, we take a look at the day-night temperature anomaly, as a proxy for the atmospheric thermal tides generated by the sun insolation diurnal cycle. The GCMv6 simulation offers a very convincing anomaly structure, especially in tropical mid-altitudes (100Pa-3Pa), even though the phasing of the tides remains a bit off, as illustrated on one month (L_S 210°-240°) in Figure 15.

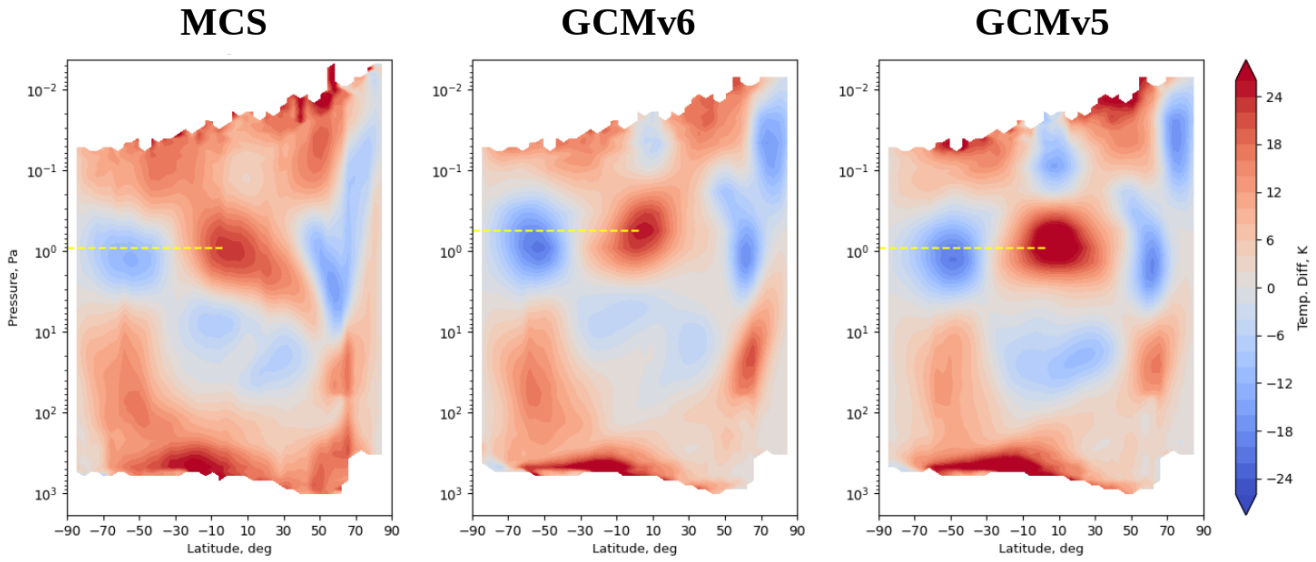

Figure 15: Diurnal temperature anomaly from MCS and GCM simulations - Zonal & time average between L_S 210° and 240° - MY29. **Left to right** : MCS ; GCMv6 ; GCMv5. The yellow dashed line points at the local maximum of the anomaly, in order to better evaluate the wave vertical phase.

Conclusion

The dust cycle is one of the main driver of the Martian climate. Its contribution to the radiative transfer, via absorbing and scattering the sun radiations, emitting in thermal infrared, or changing the ground albedo, affects the surface temperature as well as the thermal structure of the atmosphere, and therefore the circulation, at both local and global scales. Since particles serve as nucleii for the condensible species, namely water vapor and CO_2, the dust atmospheric distribution can also interact with the microphysics and impact the formation of clouds. It is thus essential to correctly characterize the dust cycle in a model of the Martian atmosphere. This is especially true as the version 6 of the PCM aims for a dust modeling that is more closely linked than before to physical processes, instead of mainly relying on external forcings.

The PCM dust cycle is now driven by the combination of three main parametrizations, that are the realistic injection following the daily scenarios, the rocket dust storms, and the mountain top flows. We go from a GCMv5 strict daily renormalization of the dust column, to a GCMv6 small radiative adjustment safeguard, that lets the dust freely evolve in the atmosphere according to the physical processes and the dynamics. The two-moment scheme, used in the model to transport the dust particles and keep track of its effective size, has also enabled a better conversion of the dust scenario forcings from infrared absorption to visible extinction. This was critical when appraising the new dust cycle with the scope of multiple diagnoses that directly or indirectly affect each other (dust mass and opacities at different wavelengths, temperature). We also implemented the scavenging of the dust and water ice by the CO_2 snow, thus making a step toward the coupling of the three physical cycles that drive the current Mars climate.

These changes resulted in numerous improvements on the dust atmospheric distribution and evolution, as well as the thermal structure, in regard to observations. Some persisting biases, like the dusty season temperature, still leave room for progress in modeling correctly the dust contribution to the Martian climate. Nevertheless, we base the production of the Mars Climate Database 6.1 on this configuration of the dust cycle, coupled with the improvements of the water cycle and the non-orographic gravity waves that are detailed in the companion technical notes of this document.

References

Bertrand, T., Wilson, R. J., Kahre, M. A., Urata, R., and Kling, A. (2020). Simulation of the 2018 Global Dust Storm on Mars Using the NASA Ames Mars GCM: A Multitracer Approach. *Journal of Geophysical Research (Planets)*, 125(7):e06122.

Chatain, A., Spiga, A., Banfield, D., Forget, F., and Murdoch, N. (2021). Seasonal Variability of the Daytime and Nighttime Atmospheric Turbulence Experienced by InSight on Mars. *Geophys. Res. Lett.*, 48(22):e95453.

Christensen, P. R., Bandfield, J. L., Hamilton, V. E., Ruff, S. W., Kieffer, H. H., Titus, T. N., Malin, M. C., Morris, R. V., Lane, M. D., Clark, R. L., Jakosky, B. M., Mellon, M. T., Pearl, J. C., Conrath, B. J., Smith, M. D., Clancy, R. T., Kuzmin, R. O., Roush, T., Mehall, G. L., Gorelick, N., Bender, K., Murray, K., Dason, S., Greene, E., Silverman, S., and Greenfield, M. (2001). Mars Global Surveyor Thermal Emission Spectrometer experiment: Investigation description and surface science results. *J. Geophys. Res.*, 111:23823–23872.

Christensen, P. R., Jakosky, B. M., Kieffer, H. H., Malin, M. C., McSween, Harry Y., J., Nealson, K., Mehall, G. L., Silverman, S. H., Ferry, S., Caplinger, M., and Ravine, M. (2004). The Thermal Emission Imaging System (THEMIS) for the Mars 2001 Odyssey Mission. , 110(1):85–130.

Forget, F., Hourdin, F., and Talagrand, O. (1998). CO_2 snow fall on Mars: Simulation with a general circulation model. *Icarus*, 131:302–316.

Goldenson, N., Desch, S., and Christensen, P. (2008). Non-equilibrium between dust and gas temperatures in the Mars atmosphere. *Geophys. Res. Lett.*, 35:8813–+.

Haberle, R. M., Kahre, M. A., Bertrand, T., Hartwick, V. L., Wilson, R. J., Wolff, M. J., and Batterson, C. (2022). Modeling Studies of Dust/Gas Non-Thermal Equilibrium in the Martian Atmosphere. In *Seventh International Workshop on the Mars Atmosphere: Modelling and Observations*, page 1404.

Hourdin, F. and Armengaud, A. (1999). Test of a hierarchy of finite-volume schemes for transport of trace species in an atmospheric general circulation model. *Mon. Wea. Rev.*, 127:822–837.

Kleinböhl, A., Schofield, J. T., Abdou, W. A., Irwin, P. G. J., and de Kok, R. J. (2011). A single-scattering approximation for infrared radiative transfer in limb geometry in the Martian atmosphere. *Journal of Quantitative Spectroscopy and Radiative Transfer*, 112:1568–1580.

Kleinböhl, A., Schofield, J. T., Kass, D. M., Abdou, W. A., Backus, C. R., Sen, B., Shirley, J. H., Lawson, W. G., Richardson, M. I., Taylor, F. W., Teanby, N. A., and McCleese, D. J. (2009). Mars Climate Sounder limb profile retrieval of atmospheric temperature, pressure, and dust and water ice opacity. *Journal of Geophysical Research (Planets)*, 114:10006.

Law, E. and Day, B. (2017). Mars Trek: An Interactive Web Portal for Current and Future Missions to Mars. In *European Planetary Science Congress*, pages EPSC2017–99.

Määttänen, A., Fouchet, T., Forni, O., Melchiorri, R., Forget, F., Savijarvi, H., Bibring, J. P., Langevin, Y., Gondet, B., Formisano, V., and Giuranna, M. (2009). A study of the properties of a local dust storm with Mars Express OMEGA and PFS data. *Icarus*, 201(2):504–516.

Määttänen, A., Vehkamäki, H., Lauri, A., Merikallio, S., Kauhanen, J., Savijärvi, H., and Kulmala, M. (2005). Nucleation studies in the Martian atmosphere. *Journal of Geophysical Research (Planets)*, 110:2002.

Madeleine, J.-B., Forget, F., Millour, E., Montabone, L., and Wolff, M. J. (2011). Revisiting the radiative impact of dust on Mars using the LMD Global Climate Model. *Journal of Geophysical Research (Planets)*, 116:11010.

Martikainen, J., Gómez-Martín, J. C., Muñoz, O., Jardiel, T., Peiteado, M., Vidrio, Y., and Wolff, M. (2022). Retrieval of Optical Constants at UV-VIS-NIR for Martian Dust Analogues by Modelling Light Scattering. In *Seventh International Workshop on the Mars Atmosphere: Modelling and Observations*, page 1562.

McCleese, D. J., Schofield, J. T., Taylor, F. W., Calcutt, S. B., Foote, M. C., Kass, D. M., Leovy, C. B., Paige, D. A., Read, P. L., and Zurek, R. W. (2007). Mars Climate Sounder: An investigation of thermal and water vapor structure, dust and condensate distributions in the atmosphere, and energy balance of the polar regions. *Journal of Geophysical Research (Planets)*, 112(E11):5–+.

Montabone, L., Forget, F., Millour, E., Wilson, R. J., Lewis, S. R., Cantor, B., Kass, D., Kleinböhl, A., Lemmon, M. T., Smith, M. D., and Wolff, M. J. (2015). Eight-year climatology of dust optical depth on Mars. *Icarus*, 251:65–95.

Montabone, L., Spiga, A., Kass, D. M., Kleinböhl, A., Forget, F., and Millour, E. (2020). Martian Year 34 Column Dust Climatology from Mars Climate Sounder Observations: Reconstructed Maps and Model Simulations. *Journal of Geophysical Research (Planets)*, 125(8):e06111.

Spiga, A., Faure, J., Madeleine, J.-B., Määttänen, A., and Forget, F. (2013). Rocket dust storms and detached dust layers in the Martian atmosphere. *Journal of Geophysical Research (Planets)*, 118:746–767.

Vals, M. (2019). *Numerical modeling of the water and dust cycles of the planet Mars and their couplings*. PhD manuscript, Sorbonne Université, Paris. https://hal.archives-ouvertes.fr/tel-02466083 (in French).

Van Leer, B. (1977). Towards the ultimate conservative difference scheme : IV. a new approach to numerical convection. *J. Computational Phys.*, 23:276–299.

Wang, C., Forget, F., Bertrand, T., Spiga, A., Millour, E., and Navarro, T. (2018). Parameterization of Rocket Dust Storms on Mars in the LMD Martian GCM: Modeling Details and Validation. *Journal of Geophysical Research (Planets)*, 123(4):982–1000.

Wolff, M. J., Smith, M. D., Clancy, R. T., Arvidson, R., Kahre, M., Seelos, F., Murchie, S., and Savijärvi, H. (2009). Wavelength dependence of dust aerosol single scattering albedo as observed by the Compact Reconnaissance Imaging Spectrometer. *Journal of Geophysical Research (Planets)*, 114(E13):0–+.